



Engineering a nanoantibiotic system displaying dual mechanism of action

Huihua Xing^{a,1} 📵, Luana Janaína de Campos^{a,1} 📵, Aramis Jose Pereira^a, Maria Mercedes Fiora^{b,c,d}, Fabio Aguiar-Alves^e, Mario Tagliazucchi^{c,d} 📵, and Martin Conda-Sheridan^{a,2}

Edited by Monica Olvera de la Cruz, Northwestern University, Evanston, IL; received December 9, 2023; accepted March 4, 2024

In recent decades, peptide amphiphiles (PAs) have established themselves as promising self-assembling bioinspired materials in a wide range of medical fields. Herein, we report a dual-therapeutic system constituted by an antimicrobial PA and a cylindrical protease inhibitor (LJC) to achieve broad antimicrobial spectrum and to enhance therapeutic efficacy. We studied two strategies: PA-LIC nanostructures (Encapsulation) and PA nanostructures + free LJC (Combination). Computational modeling using a molecular theory for amphiphile self-assembly captures and explains the morphology of PA-LJC nanostructures and the location of encapsulated LJC in agreement with transmission electron microscopy and two-dimensional (2D) NMR observations. The morphology and release profile of PA-LJC assemblies are strongly correlated to the PA:LJC ratio: high LJC loading induces an initial burst release. We then evaluated the antimicrobial activity of our nanosystems toward gram-positive and gram-negative bacteria. We found that the Combination broadens the spectrum of LJC, reduces the therapeutic concentrations of both agents, and is not impacted by the inoculum effect. Further, the *Encapsulation* provides additional benefits including bypassing water solubility limitations of LJC and modulating the release of this molecule. The different properties of PA-LJC nanostructures results in different killing profiles, and reduced cytotoxicity and hemolytic activity. Meanwhile, details in membrane alterations caused by each strategy were revealed by various microscopy and fluorescent techniques. Last, in vivo studies in larvae treated by the Encapsulation strategy showed better antimicrobial efficacy than polymyxin B. Collectively, this study established a multifunctional platform using a versatile PA to act as an antibiotic, membrane-penetrating assistant, and slow-release delivery vehicle.

antimicrobial | dual therapy | peptide amphiphiles | nanostructures

A main health challenge is the ongoing antimicrobial resistance (AR) crisis (1). The various infectious diseases outbreaks of the 21st century have severely impacted livelihoods globally (2). This problem is aggravated by the imbalance between the escalating need for therapeutic options and the very limited supply of antimicrobial agents under development (3). Thus, the search for novel therapies to meet this challenge is of paramount importance.

Peptide amphiphiles (PA) are self-assembling compounds that display a wide range of biomedical applications (4). Among these, their antimicrobial potential is of particular interest. The mechanism of action of PA nanostructures shares similarities with antimicrobial peptides (AMP), involving the insertion into and disruption of bacterial membranes (5). Despite the crucial role of the interaction between PAs and biological membranes in their biological activities (6), the underlying mechanism of action is not completely understood.

A main difference between PAs and AMPs lies in the alkylation of the N terminus in the former, contributing to enhanced metabolic stability when compared to the latter (7). Further, PA nanostructures offer the possibility to encapsulate small molecules (8), proteins and stem cells (9), resulting in a similar biodistribution profile of the cargo and the nanocarrier. It has been suggested that fiber-shape PA assemblies offer advantages such as high encapsulation efficiency, prolonged circulation time, and improved specific accumulation compared to nanostructures with alternative morphologies (10). Furthermore, the PAs with positive charges (cationic PAs) exhibit similar characteristics to cell-penetrating peptides, facilitating greater and faster accumulation in the target (11). On the other hand, our team and others have demonstrated that spherical cationic PA nanostructures can work as potent antibacterial agents (12, 13). In the current study, we sought to extend our investigation by evaluating the potential of PA nanostructures as an active delivery platform (nanoantibacterial) for the treatment of infections. As a proof-of concept, we described a dual [C₁₆u]K₂-LJC 1-26 (PA–LJC) antimicrobial therapy. The PA, $[C_{16}]uK_2$, consists of a sixteen-carbon tail ($[C_{16}]$) tail to provide hydrophobic interactions with membranes and a lipophilic core, a urea linker

Significance

The lack of new antibacterials has complicated our ability to deal with antimicrobial resistance. It is key to develop alternative approaches to combat pathogenic infections. Herein, we present a nanoantibacterial therapy that combines two molecules with orthogonal mechanism of action: a disruptor of cylindrical proteases (new mechanism of action) and a nanocarrier that damages the bacterial membrane. Notably, upon disassembly, the nanocarrier becomes an active component of the antimicrobial therapy, transforming the narrow-spectrum small molecule (limited permeation) into a broad-spectrum compound. Further, the antibacterial effect and cytotoxicity profile is altered based on how the therapy is formulated: coadministration of the molecule vs. encapsulation of the small molecule into the nanocarrier.

Author contributions: H.X., L.J.d.C., M.T., and M.C.-S. designed research; H.X., L.J.d.C., A.J.P., M.M.F., F.A.-A., and M.T. performed research; F.A.-A., M.T., and M.C.-S. contributed new reagents/analytic tools; H.X., L.J.d.C., M.M.F., F.A.-A., M.T., and M.C.-S. analyzed data; and H.X., L.J.d.C., M.M.F., F.A.-A., M.T., and M.C.-S. wrote the paper.

The authors declare no competing interest.

This article is a PNAS Direct Submission.

Copyright © 2024 the Author(s). Published by PNAS. This article is distributed under Creative Commons Attribution-NonCommercial-NoDerivatives License 4.0 (CC BY-NC-ND).

¹H.X. and L.J.d.C. contributed equally to this work.

²To whom correspondence may be addressed. Email: martin.condasheridan@unmc.edu.

This article contains supporting information online at https://www.pnas.org/lookup/suppl/doi:10.1073/pnas. 2321498121/-/DCSupplemental.

Published April 9, 2024.

to increase cohesion via H-bonding, and two Lysine residues to achieve electrostatic interactions with membranes (for more details on the rationale used to select $[C_{16}]uK_2$, see "Design of PA," in SI Appendix). LJC 1-26 (referred to from now on as LJC) is a dihydrothiazepine which targets the ClpX chaperone of the caseinolytic protease proteolytic (ClpXP) complex, halting its functions (14). The ClpXP degradation machinery is key to bacteria cell homeostasis (15) and virulence (16). Unfortunately and according to our assays, LJC displays antimicrobial activity only against gram-positive strains. Since ClpXP is conserved in most bacteria (ClpXP is the most ubiquitous of the Clp proteases) (17), we theorize that the lack of antimicrobial activity against gram-negative species is due to poor permeability rather than lack of target engagement (14, 18, 19).

In this study, we undertook an examination and comparative analysis of two dual therapeutic modalities: Combination and Encapsulation. In the Combination (adjuvant-like) strategy, the preformed PA nanostructures and free LJC were freshly mixed and administered. The anticipated outcome involves the modification of membrane permeability by PA, facilitating the passage of the LJC molecule across the bacterial membrane and subsequent targeting of the ClpXP system (of course other targets may be affected too). In the Encapsulation approach, PA-LJC nanostructures were prepared, with the PA serving as a nanocarrier for the hydrophobic small molecule. In both cases, a synergistic/ additive effect is achieved, manifesting as a reduction in the dosage of both LJC and PA. Consequently, the involvement of PA in the therapeutic process is characterized by an active role, distinct from its conventional function as an inert nanocarrier.

We studied the morphology of PA and PA-LJC nanostructures by transmission electron microscopy (TEM) and computer modeling

using a molecular theory (MOLT) for amphiphile self-assembly. To assess the antimicrobial activity, we determined the minimal inhibitory concentration (MIC), performed live/dead assays, and an inoculum effect (IE) inhibition test. The release rate of LJC from the nanostructures was experimentally and theoretically studied. MOLT calculations elucidated that assemblies with a high load of LJC are metastable structures concerning the release of LJC. In other words, at higher concentrations of encapsulated LJC, the nanostructures are less stable and more prone to release the cargo molecule. These calculations provided insights into the thermodynamic aspects governing the rates of LJC release. To evaluate bacterial membrane integrity after treatment, we studied propidium iodine (PI) uptake and used various microscopy techniques. The cytotoxicity of the two dual therapies was analyzed using HEK 293 T, HEp2, and red blood cells. Finally, we conducted in vivo studies with Galleria mellonella larvae to obtain an initial evaluation of the potential of our dual therapy to treat infectious diseases.

Results

Characterization of PA-LJC Encapsulated Nanostructures. Morphology study of encapsulated nanostructures. After 24 h, the PA molecules assembled into elongated structures in aqueous environment (Fig. 1A). Nevertheless, the encapsulation of LJC induced a morphological transition, which was observed by

TEM, shifting from fibers to shorter fibers and ultimately forming micelles at the same time point (methods and characterization can be found in SI Appendix, Figs. S1-S6 and Scheme S1). The encapsulation, inside 16 µg/mL of the PA, of 0.5 µg/mL of LJC (32:1 ratio) results in the coexistence of long and short nanofibers.

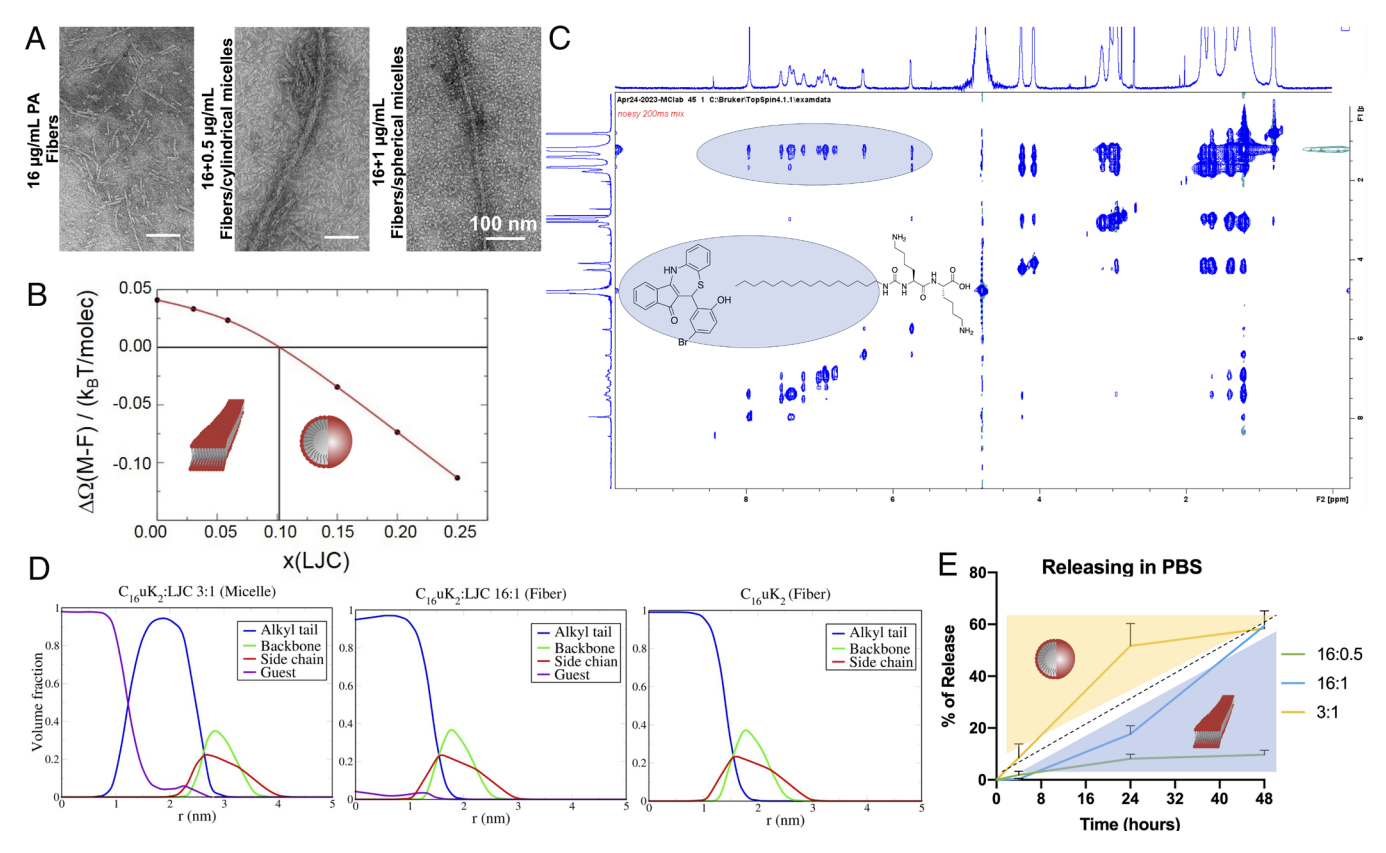


Fig. 1. (A) TEM micrographs of PA in water (pH 7) at 16 μg/mL, encapsulated PA-LJC at 16 + 0.5, and encapsulated PA-LJC at 16 + 1 μg/mL. (Scale bar, 100 nm.) (B) Free energy difference between micelle and elongated assemblies as a function of the molar fraction of LJC at pH = 7. (C) NOESY spectrum highlights the cross-peaks (circled in blue) between hydrophobic portions of PA and aromatic region of LJC. (D) Volume fraction PA and LJC as a function of the distance to the center of the micelles and central axis of the fibers for pH = 7. The PA:LJC mass ratio and predicted equilibrium morphology are indicated for each plot. (E) LJC release kinetics in PBS.

Conversely, spherical micelles are observed when 1 µg/mL of LJC was encapsulated into the same amount of PA (16:1 ratio). Furthermore, a reduction in the zeta potential is noted at this concentration (SI Appendix, Fig. S7).

Encapsulation at a 6:1 (weight ratio) of PA:LJC formed a mixture of micelles and ultrashort fibers (less than 50 nm length). However, the 3:1 encapsulation exhibited the formation of short fibers/cylindrical micelles with lengths ranging from 50 to 100 nm. (SI Appendix, Fig. S8). Further, we performed a morphological kinetic study, at the lowest concentrations, at 1 h and 4 h. We found the same morphologies are observed at 1 h, 4 h, and 24 h. The only difference is that the 3:1 PA:LJC system displayed slightly longer, needle-like fibers after 1 h.

To understand the morphological transition when the PA/LJC ratio changes, we modeled the molecular organization of the assemblies using MOLT, a thermodynamics-based coarse-grained statistical model that can predict the structure and stability of assemblies based on the molecular structure of the amphiphiles and encapsulated molecule and the properties of the solution [i.e. pH, ionic strength (details in SI Appendix, Fig. S9 and Tables S1 and S2)] (20). Fig. 1B shows the difference between the free energies of the most stable micelle and fiber morphologies at pH 7 as a function of the molar LJC:PA ratio in the aggregate $[\Delta\Omega]$ denotes the free energy difference, Ω is a semigrand canonical free energy (21, 22)]. The plot indicates that the predicted morphology of PA nanostructures, when encapsulating low LJC concentrations, favors a fiber structure. However, an increase in LJC concentration shifts the preference toward the spherical morphology. The fiber-tomicelle transition can be attributed to the augmentation of aggregation size and the associated decrease of surface curvature of the assembly caused by the encapsulation of LJC molecules into the fibers (23). The change in local curvature triggers a transition to micelles to optimize the packing of the PA molecules. The fiber-tosphere transition is predicted to occur at a molar fraction of LJC (x(LJC)) of ~0.1. The mass ratios (in mg LJC/mg PA) of 16:0.5, 16:1, 6:1, and 3:1 correspond to x(LJC) = 0.037, 0.072, 0.140 and 0.293. Therefore, the 16:0.5 and 16:1 are predicted to be nanofibers and the 6:1 and 3:1 are expected to form micelles. This prediction follows the observed trend regarding the morphology of the nanostructures and the amount of encapsulated LJC seen by TEM (further details on the correlation between MOLT and TEM can be found in SI Appendix, Fig. S6 and Morphology Study of Encapsulated Nanostructures).

Encapsulation Study.

Internal arrangement in nanostructures. As described, the encapsulation of LJC affects the morphology, and thus, may influence the properties of PA nanostructures (24). We used Diffusion Ordered Spectroscopy to study the diffusion coefficient (D) of the PA-LJC nanostructure and to assess LJC encapsulation (25). We obtained similar D values for PA and LJC, which suggests that these two species are within the same entity in solution (details in SI Appendix, Fig. S10). Then, we performed a Nuclear Overhauser Effect Spectroscopy (NOESY) experiment (Fig. 1C and SI Appendix, Fig. S10) to study the distance between LJC and the PA to assess the distribution of LJC in the nanostructures (25). Cross-peaks between the aromatic region of LJC and the alkyl regions of PA were found, indicating that LJC and the PA alkyl segment (and/or the side chain of Lys residues) are located within a short distance (<5 Å). TEM and NMR studies on Combination strategy were performed to compare the molecular arrangements with Encapsulation strategy (details shown SI Appendix, Figs. S11-S13 and Combination Strategy Studies).

Subsequently, MOLT was employed to further access the internal molecular organization of the nanostructures. Fig. 1D shows the predicted volume fraction of the PA and LJC as a function of the distance to the center of the aggregates (center of the micelle or central axis of the fiber) for the mass ratios PA:LJC used in the experiments. As expected, the alkyl tails of the PAs are at the core of the assembly and the backbone and side chains form the corona. Consistent with the NMR experiments, the LJC molecules are predicted to be located at the core of the nanostructures due to their hydrophobicity, whether in fibers or spherical micelles.

PA/LJC ratio influences the releasing profile. The supramolecular morphology is critical for the release of cargo (26). Therefore, we investigated the release behavior associated with three different PA/LJC ratios under two conditions: 1) phosphate-buffered saline (PBS), and 2) dichloromethane (DCM)/H₂O. The drug release in PBS was evaluated by a filtration-lyophilization method (Fig. 1*E*), described in SI Appendix, Figs. S15 and S16. In the case of 16 + 0.5 mg/mL and 16 + 1 mg/mL (PA + LJC, nanofibers), a similar slow release was observed until 24 h. However, the 16 + 1 mg/ mL system shows a significant increase in release from 24 h to 48 h (15 to 60%), compared to nanostructures made of 16 + 0.5mg/mL. In contrast, 3 + 1 mg/mL (micelles) exhibit a fast release (around 60%), compared to their fibrous counterparts, in the first 24 h, reaching a plateau during the next 24 h. In addition, we designed a biphasic DCM/H₂O method seeking to mimic the transfer of the LJC, encapsulated in the nanostructures, from aqueous phase into a lipid phase (membranes). A LJC release profile similar to the one seen on the PBS method was observed (SI Appendix, Figs. S17 and S18).

To understand the driving force behind the release of LJC from the aggregates, we estimated the free energies of the three species (PA, LJC, PA–LJC) and calculated the free energy change ($\Delta\Omega$) involved in the release. For the PA:LJC mass ratios of 16:0.5, 16:1, and 3:1, we calculated a $\Delta\Omega$ = -4.5, -5.2, and -6.1 $k_{\rm B}$ T/molecule (see *SI Appendix*, Table S1 for information). These results indicate: 1) for these three experimental systems, the PA_nLJC_m aggregates are predicted to be thermodynamically unstable with respect to the release of the drug, which is consistent with the observation of spontaneous LJC precipitation from solution over time (Fig. 1E), and 2) the free energy of release of LJC becomes more negative when the PA:LJC ratio decreases (more LJC molecules in the core), suggesting that micelles with higher content of LJC are more unstable. This may explain the experimental observation that the LJC releasing rate increases when the PA:LJC ratio decreases. In summary, our findings indicate that increasing the amount of loaded LJC leads to two effects: a reduction in the stability of nanostructures with respect to the LJC release and a stabilization of spherical micelles relative to fibers. These observations may explain the faster release of LJC from micelles when compared to fibers (Fig. 1*E*).

Antimicrobial Activity Evaluations.

Improved antimicrobial efficacy reached by dual therapy. We determined the MIC and the Minimal Bactericidal Concentration (MBC) of the individual PA and LJC molecules against one grampositive (Methicillin-resistant Staphylococcus aureus, MRSA, JE2) and one gram-negative bacterium (Acinetobacter baumannii, patient isolated) (SI Appendix, Table S3). The PA presents intermediate antimicrobial activity against both bacteria (MIC: 32 µg/mL). Meanwhile, LJC presents activity comparable to Daptomycin (Dapto) against MRSA JE2 (MIC: 2 µg/mL) and no activity against A. baumannii (a more detailed report on LJC activity and mechanism of action is under preparation).

Then, we evaluated and compared the antimicrobial activity of the two designed strategies (Fig. 2A). In the Combination approach, the PA nanostructures were first assembled without the addition of LJC (the process is illustrated in Fig. 2A and SI Appendix, Experimental section). Subsequently, the antimicrobial assays were performed immediately after mixing PA and LJC (negligible LJC encapsulation is expected, as described in *Combination* study shown in SI Appendix, Combination Strategy Studies). A checkerboard assay reveals that the *Combination* therapy leads to a decrease in MICs of both PA and LJC against MRSA JE2 (Fig. 2B). The MIC_{PA} is reduced from 32 $\mu g/mL$ to 2 $\mu g/mL$ and MIC_{LJC} from 2 $\mu g/mL$ to 1 µg/mL. The calculated fractional inhibitory concentration index (FICi) (27) against MRSA JE2 is 0.56, indicating an additive effect (28). No change in the MIC is observed when LJC is combined with Dapto (SI Appendix, Fig. S19). In the case of A. baumannii, the Combination strategy (Fig. 2C) similarly yielded a

reduced MIC for the PA (from 32 µg/mL to 16 µg/mL) when combined with 1 µg/mL of LJC. Notably, LJC alone is inactive against gram-negative species.

For the *Encapsulation* approach, the LJC and PA molecules were mixed, annealed, and aged to prepare PA–LJC nanostructures (the process is illustrated in Fig. 2A and SI Appendix, Experimental section), followed by dilution in Mueller-Hinton Broth (MHB had negligible influence on the morphology, as shown in SI Appendix, Fig. S14). To determine the MIC $_{Encap}$, we tested different PA–LJC concentrations (SI Appendix, Fig. S20). For both bacteria tested, the resulting MIC for this strategy is $14 \, \mu g/m L_{(PA)} + 0.5 \, \mu g/m L_{(LJC)}$, showing an additive effect (FiCi = 0.69) for MRSA JE2 and a spectrum broadening of LJC against A. baumannii. The observed increase in the MIC for MRSA JE2 in the Encapsulation approach compared to the Combination strategy (2 + 1 $\mu g/m L$) may be due to a required minimum PA concentration to allow effective

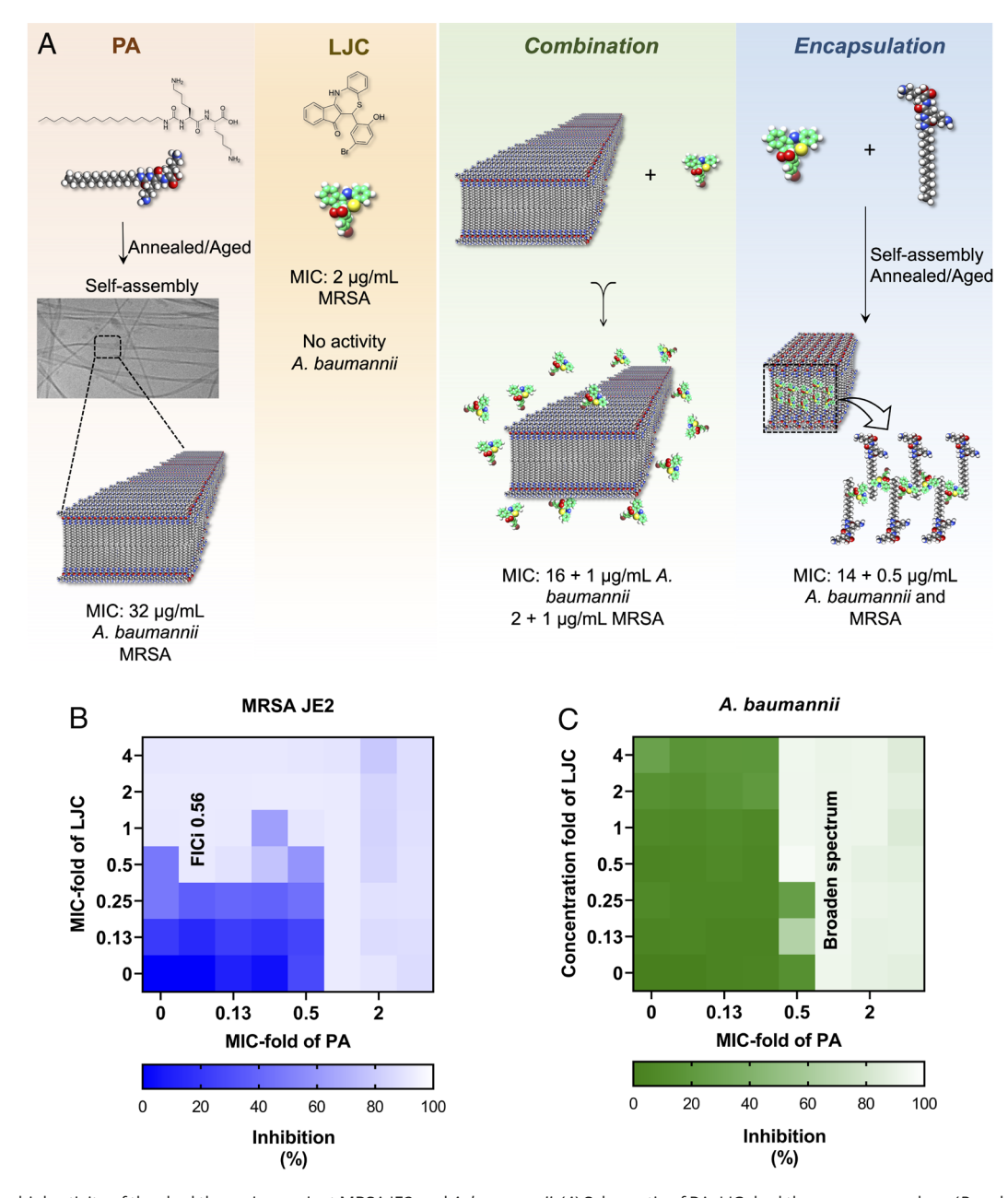


Fig. 2. Antimicrobial activity of the dual therapies against MRSA JE2 and *A. baumannii*. (*A*) Schematic of PA–LJC dual therapy approaches; (*B* and *C*) Checkerboard results for the *Combination* strategy against MRSA JE2 and *A. baumannii*. The tests were performed using a bacteria density of 1.5 × 10⁵ CFU/mL. Two biological replicates were analyzed. *Note: In panel *A*, the cartoons of the fibers are used for illustrative purposes. The cartoons show a specific portion of whole fibers (twisting is not drawn) obtained from TEM images at 16 mg/mL.

encapsulation. Notably, the molecular volume difference between PA and LJC is small (1,820.5 and 1,012.5 cm³/mol). Thus, a minimum quantity of PAs is required to form a sufficiently large hydrophobic core to entrap LJC molecules. It is noteworthy that the MIC_{LJC} against MRSA JE2 and *A. baumannii* for the Encapsulation strategy is reduced when compared to the Combination approach (1 $\mu g/mL$ to 0.5 $\mu g/mL$).

In conclusion, both dual therapies resulted in a MIC reduction and a spectrum broadening for LJC. Additionally, the PA:LJC ratio for the determined MIC $_{Encap}$ (14:0.5 μ g/mL) promotes fiber formation, as demonstrated in the morphology study, and predicted by MOLT. At this ratio, a slow release of LJC is expected (PA as well, detailed explanation provided in the *Discussion* section).

Live/dead assay reveals distinguish killing profiles. To determine the killing profile of our dual therapies, a cell viability analysis was performed using *A. baumannii* stained with PI and DAPI. Dead bacterial cells (PI positive), can be distinguished from live bacteria with intact membranes (PI negative) by PI uptake vs. exclusion (29). Flow cytometry analysis (Fig. 3A) was used to quantitatively study the percentages of live and dead cells within the samples, while confocal laser microscopy (Fig. 3B) was used to qualitatively analyze the antimicrobial profile of our strategies.

The flow cytometry and confocal analysis confirmed the results observed in the MIC/MBC determination. At 2× MIC (64 µg/ mL, the MBC concentration), PA alone eliminates >98% of bacterial cells (Fig. 3A). At the PA-MIC, around 34% of dead cells are observed. Regarding the dual therapies, we observed a difference in the killing profile between the Combination and Encapsulation strategies. The Combination approach resulted in over 45% of bacterial death at 2× MIC (32 + 2 µg/mL). In contrast, at 2× MIC (28 + 1 µg/mL), the Encapsulation strategy resulted in less than half death of the Combination strategy (~20%) cell death). The difference in killing profiles within 6 h between the two strategies may be related to the number of free LJC and PA molecules in solution, with more free molecules available in the Combination than in Encapsulation (slow release) strategy. Therefore, the formulation can modulate the release of both PA and LJC, altering the antimicrobial activity profile. A more detailed explanation is given in the *Discussion* section.

Mode of Action.

Membrane mechanistic studies reveal membrane damage. While the PA (alone), *Combination* and *Encapsulation* strategies all target bacterial membranes, we postulate potential distinctions in their

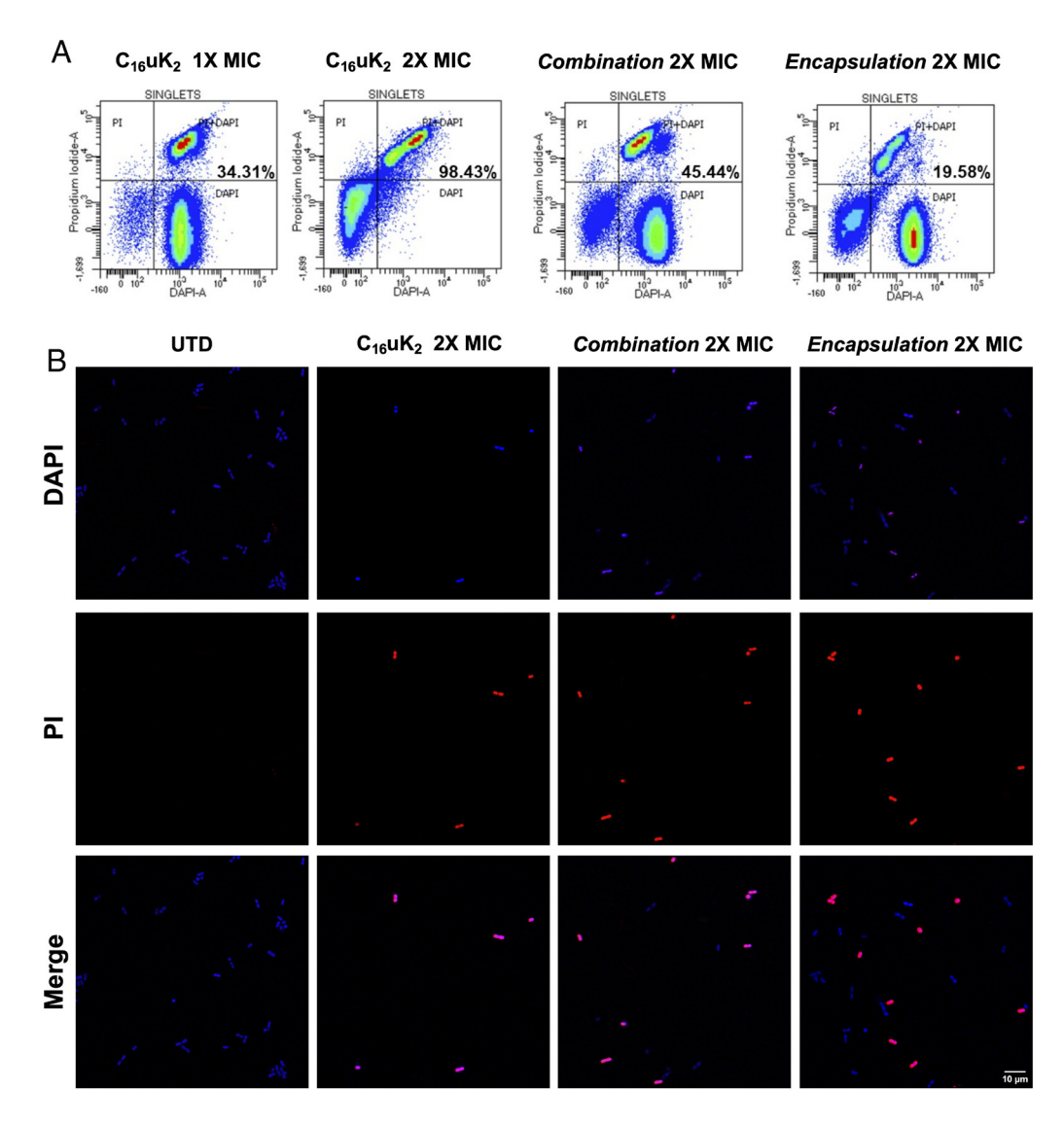


Fig. 3. Live/dead analysis using *A. baumannii* after 6 h of treatment. (*A*) Flow cytometry, and (*B*) Confocal laser microscopy. PI+DAPI-positive signal indicates dead cells, and DAPI-only positive signal represents live cells. UTD: untreated (PBS) control. Individual PA MIC: 32 μg/mL; *Combination* strategy MIC: 16 (PA) + 1 (LJC) μg/mL; *Encapsulation* strategy MIC: 14 (PA) + 0.5 (LJC) μg/mL.

killing profiles and, more likely, in the specific alterations induced in the bacterial membrane. To assess the impact of our dual therapies on bacterial membranes, we evaluated the membrane permeability (PI uptake assay) and membrane depolarization [voltage-sensitive dye DiSC3(5) assay] induced by our proposed structures (Fig. 4 A and B). Comparatively, higher membrane permeability is observed with the PA alone and in the *Combination* approach when contrasted with the *Encapsulation* strategy. In addition, the data indicate that the membrane permeability change induced by the polymyxin B (PMB) control aligns with the alterations observed in the PA alone or the *Combination* (Fig. 4A). Further, a similar alteration of membrane potential was observed when bacteria were treated with PA or PMB (both are cationic amphiphiles). On the other hand, the Encapsulation strategy caused a smaller change in the membrane potential (Fig. 4B). This observation agrees with our live/dead analysis, in which the PA or the Combination strategy caused higher percentages of cell death compared to the *Encapsulation* approach (during the same treatment time). Noteworthy, no change in membrane permeability or potential is observed when A. baumannii was treated with LJC alone.

To further determine whether the change in the membrane voltage observed for the Encapsulation strategy was significant enough to induce a change in bacterial surface charge, we evaluated the bacterial zeta potential (Fig. 4C). Interestingly, the Encapsulation approach induced a more pronounced increase in the bacterial zeta potential than the PA nanostructures alone. In contrast, PMB did not exhibit significant changes in the bacterial zeta potential. This observation may be associated with PMB's mode of action, wherein it displaces essential divalent cations (such as Ca²⁺ and Mg²⁺) from their binding sites in bacterial lipopolysaccharide (30). The differences observed here might be an explanation for the lack of interaction of LJC and PMB in the checkerboard assay.

To confirm the membrane damage and gather additional information regarding the alterations caused in the membrane, we conducted scanning electron microscopy (SEM) and confocal imaging. The SEM shows membrane bubbling (indicated by yellow arrows) and debris (A. baumannii in Fig. 4D, and MRSA JE2 in SI Appendix, Fig. S21). In addition, we stained the bacterial membranes with FM4-64 dye (Fig. 4E, red color, more details in SI Appendix, Figs. S22 and S23). The red-stained bacterial membranes after treatment with PA or the two dual therapies were faded (red arrows) and heterogeneous (orange arrows), indicative of membrane alteration. However, no membrane morphology change for LJC was observed. Thereafter, atomic force microscopy (AFM) was performed to obtain profiles of the treated bacterial membranes. As observed by AFM (Fig. 4F, more details in SI Appendix, Figs. S25–S29), the untreated A. baumannii exhibits rod-shaped morphology with a smooth surface as illustrated in the height profile. It is notable that after the treatment (for only 2 h) with the PA and the two strategies, the bacterial surface exhibited roughness, as evidenced by the presence of varying heights (shown as multiple peaks and valleys in the surface height profile plots).

To further understand the changes in bacterial membranes, we used TEM (Fig. 4G). The untreated sample shows the expected rod-shape morphology for the pathogen with two distinguishable membranes [around 16 nm interval distance, pointed by yellow arrows in the untreated sample (UTD)]. Following a 2-h period, the PA-treated sample exhibited various alterations, including shrinking, low cytoplasmatic density (blue arrows), mesosome-like structures (red arrows), bubbling, coronate tubular appendages. These observations suggest membrane damage and a decrease in cell viability (Fig. 4G, more details in SI Appendix, Fig. S30). For the Combination-treated bacterial sample, similar alterations were observed when compared to the PA alone, implying the presence of PA-membrane interactions. For Encapsulation-treated bacteria, the visible occurrence of these alterations is slightly reduced compared to the other two treatments, which is expected due to the slow-release profile of PA and LJC in this strategy.

When the treatment time was extended to 6 h (Fig. 4G), an insufficient bacterial pellet was obtained, likely indicative of the PA alone nanostructures' fast-killing profile. This result agrees with the observations described above. For the Combination-treated samples, the TEM micrograph shows electron-dense spherical cytoplasmic inclusions (green arrows) with reduced intensity, predominantly located peripherally. Similar observations have been reported with PMB analogues (31). For the Encapsulation-treated samples, the membrane alterations include swollen periplasmatic space (yellow arrow), membrane waving (blue arrow), and loss of a defined membrane (orange arrow). The swelling likely results from the leakage of cellular materials from the cytoplasm, leading to an increase in the periplasmic space (4.5-times compared to untreated bacteria), which has also been reported for PMB (31). More information of these studies can be found on *SI Appendix*, Figs. S21–S30).

It has been shown that some dihydrothiazepines, as LJC, affect the expression of virulence factors (14). Since the PAs aid LJC penetration into A. baumannii, we measured the expression of genes associated with virulence and biofilm formation to investigate the intracellular effect of our *Combination* on this bacterium. This strategy was selected due to its faster action when compared to Encapsulation, aiming to avoid insufficient alteration in gene expressions. Thus, RT-qPCR was performed following biofilm growth for 24 h with 2× MIC_{comb}. Expression changes in five genes related to virulence factors and biofilm formation were observed (details in SI Appendix, Fig. S31). In particular, the gene bap showed a fivefold increase in expression when compared to the control groups. This gene is related to the adherence of A. baumannii to cell surfaces (32). Interestingly, dihydrothiazepine molecules have been shown to increase the expression of adhesins in S. aureus (14). The impact on the bap gene supports our hypothesis that the limited activity of LJC in gram-negative bacteria is attributed to inadequate penetration. In addition, it has been proven that the presence of bap protein increases the A. baumannii cell surface hydrophobicity (32). This change, considering the hydrophobic tail of PAs, may help to explain the unique alterations caused by the combination at 6 h of treatment (green arrows in Fig. 4). SI Appendix presents a further discussion on the effect of the evaluated genes.

Membrane targeting PA inhibits the IE. It is accepted that antimicrobial activity is linked to the initial density of cells used to determine the inhibition of bacterial growth (33). This phenomenon, known as the IE, can impact drug efficacy given the considerable variation in bacterial load observed across clinically relevant infections (34). To determine the impact of the dual therapies on the IE, we evaluated the MIC change using a bacterial density ranging from 10° to 108 CFU/mL (Fig. 5 *A* and *B*).

Regarding A. baumannii, for the free PA, the Combination or PMB (2 µg/mL), the MIC values inhibited bacterial growth up to 10⁸ CFU/mL while gentamicin's MIC (2 μg/mL) presented a twofold increase starting at 5×10^7 CFU/mL. For the MRSA JE2, the original MIC_{PA} value did not change up to 10⁸ CFU/mL. However, the MIC_{Comb} displayed an increase of around 2.4-fold

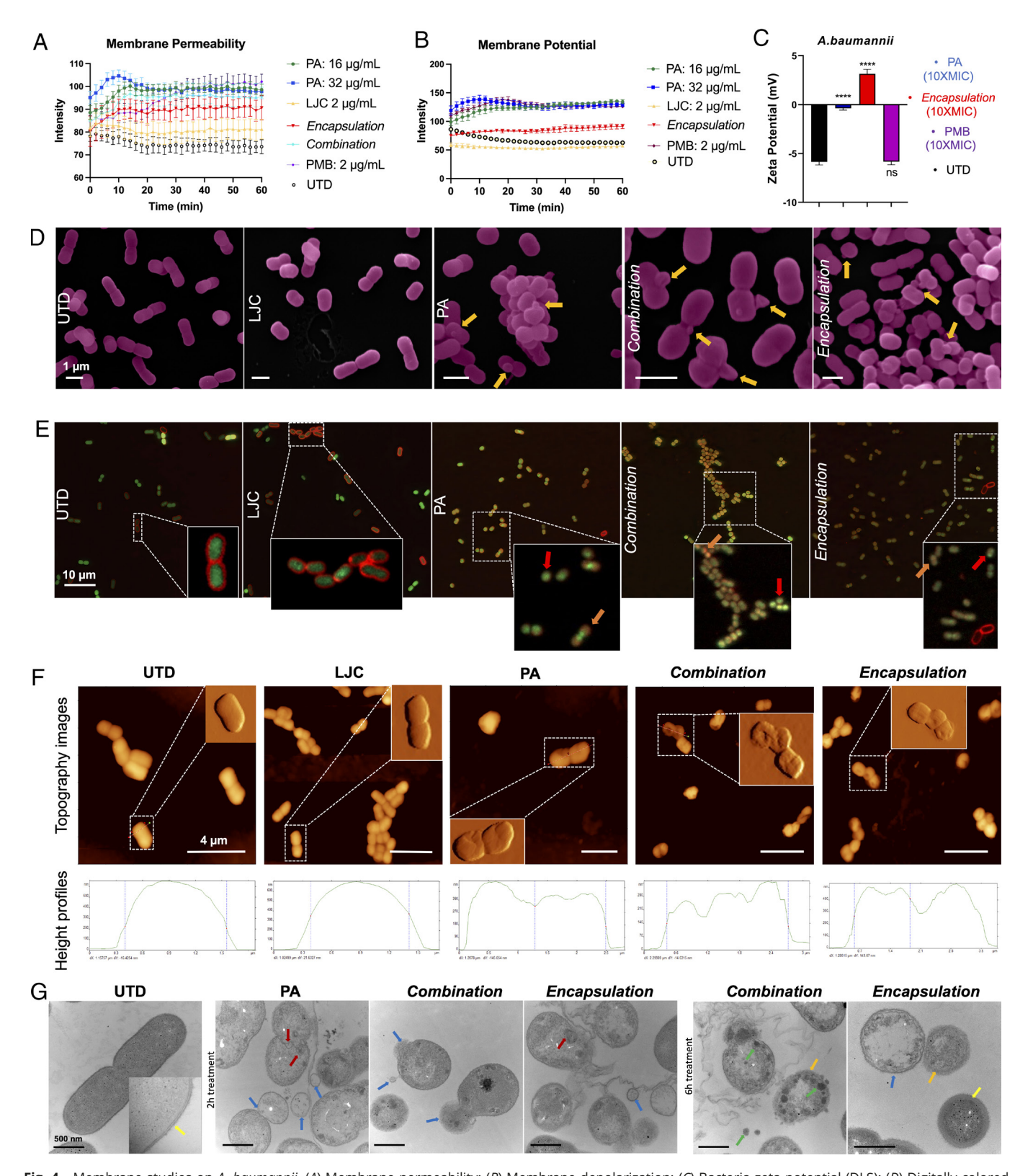


Fig. 4. Membrane studies on A. baumannii. (A) Membrane permeability; (B) Membrane depolarization; (C) Bacteria zeta potential (DLS); (D) Digitally colored SEM images of treated and untreated bacteria after 2 h of treatment; (E) Apotome confocal images stained with FM4-64 (membrane) and SYTO 9 (nucleic acid) of treated and untreated bacteria cultured for 2 h; (F) AFM topography images and height profiles of treated and untreated bacteria cultured for 2 h; (G) TEM images of treated and untreated bacteria cultured 2 h and 6 h. Red arrows point out mesosome-like structures, blue arrows mark shrinking, leaking, and losing of cytoplasmatic content, green arrows show the electron-dense inclusions, orange arrows indicate the loss of distinct membrane, and yellow arrows show the periplasm space. All microscopy studies used: LJC-2 µg/mL; PA 1× MIC; Combination 2× MIC; and Encapsulation 2× MIC.

at 10^7 CFU/mL and kept increasing up to 10^8 CFU/mL. MIC_{LJC} increases twofold at 10^6 CFU/mL, however, no increase was observed up to 108 CFU/mL. Interestingly, the controls, vancomycin (VCM) and Dapto, presented significant increases in the

MIC values as the bacterial density increases. MIC_{VCM} (0.5 µg/mL) presents a 16-fold increase at 5×10^6 CFU/mL. MIC_{Dapto} (1 μ g/mL) increases twofold at 107 CFU/mL, and an eightfold increase is observed at 108 CFU/mL.

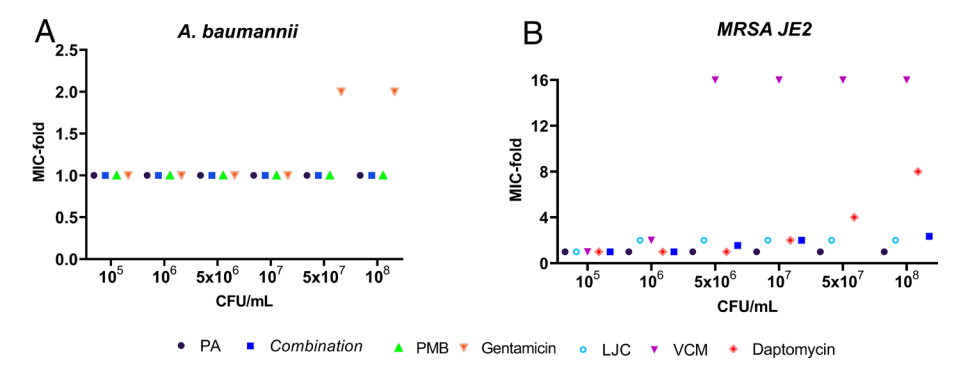


Fig. 5. The IE analysis of our proposed dual therapies. MIC values of PA, LJC, Combination and approved antibiotics against (A) A. baumannii; (B) MRSA IE2. PMB: polymyxin B; VCM: vancomycin.

The antimicrobial activity of single/combined PA for both tested strains, and LJC for MRSA JE2, is not significantly influenced by bacterial density. This result is significant because high-density bacterial infections, such as bacteremia, urinary tract infections, and endocarditis, typically exhibit bacteria densities >10' CFU/ mL (35).

Cytotoxicity and Hemolytic Activities

A challenge of AMPs is the difficulty of maintaining an acceptable therapeutic index due to their toxicity against human cells (36). Thus, we studied the cytotoxicity profile of PA, LJC, and the Combination and Encapsulation therapies against human epithelial (HEp-2, carcinoma derived) and human embryonic kidney (HEK 293T) cell lines (Fig. 6A and SI Appendix, Figs. S32 and S33).

LJC presented more than 70% viability at 128 µg/mL against both tested cell lines (SI Appendix, Fig. S32 A and B). The PA alone showed ~70% viability at 128 µg/mL (SI Appendix, Fig. S32B) against HEK293T cells but higher toxicity was observed against the cancer-derived HEp-2 cells (TC50: $42.07 \pm$ 0.6 µg/mL, SI Appendix, Fig. S32A) and mice red blood cells (HC₅₀: $40.08 \pm 0.9 \,\mu\text{g/mL}$, Fig. 6B). A higher toxicity of cationic PAs against cancer cell lines has been observed in the literature (37), an observation we have also noted with our cationic PAs (to be reported). In general, cancer cells (38) and red blood cells (39) present a more negative surface charge in comparison to normal cells. Therefore, higher toxicity of cationic PAs against these cell lines may be attributed to stronger electrostatic interaction with the cell membrane.

Next, we evaluated the cytotoxic of the dual therapies. For HEp-2 cells, an improvement in cell viability was achieved by both strategies. At 32 µg/mL the free PA presented ~57% cell

viability. By using $32 + 2 \mu g/mL$ of the *Combination* (2× MIC for A. baumannii) or Encapsulation strategies (>2× MIC against MRSA JE2 and A. baumannii), the cell viability increased to ~72% and 82%, respectively (Fig. 6A). We postulate that the change in intermolecular cohesion caused by the hydrophobic interactions between PA and LJC is responsible for the lower toxicity of the Encapsulation. Our theory is that LJC encapsulation prevents the release of PA molecules from the PA-LJC nanostructures restricting their interaction with cell membranes. Both therapies demonstrated favorable cell viability against the normal human cell line HEK 293T (*SI Appendix*, Fig. S33), when compared with HEp-2 cells, possibly due to differences in their membrane-surface charge.

The hemolytic activity followed a similar trend. At the MIC of the Encapsulation approach (14 + 0.5 µg/mL) and at 16 µg/mL of PA (concentration of PA required to reach the MIC of the combination strategy), negligible rates of hemolysis (<3%) were observed. Formulations with a hemolysis value of <10% are considered to be nonhemolytic (40). This observation indicates an improvement over the hemolytic activity of the single PA-MIC (~34% hemolysis). Collectively, the results indicate that at the MIC, high cell viability percentages could be achieved in vitro using both dual therapies.

In Vivo Acute Toxicity and Antibacterial Study (G. mellonella Model)

G. mellonella (wax moth larvae) is a cost-effective and simple in vivo model for studying antibacterial activity (41). First, we evaluated the in vivo acute toxicity of the PA, LJC, and the Encapsulation therapy over a 4-d period (42). The Combination strategy was not examined due to solubility problems at the required testing concentrations. As shown in Fig. 7A (and in

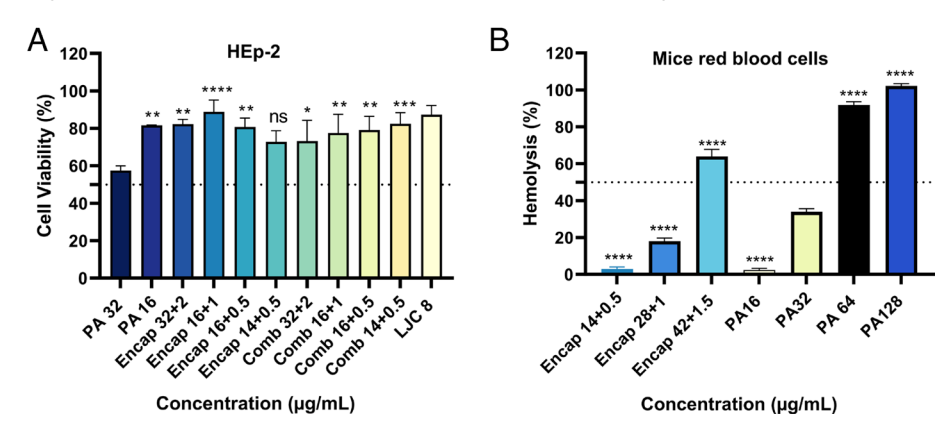


Fig. 6. Cell viability analysis of dual therapies compared with individual PA and LJC against (A) HEp-2 and (B) Mice red blood cells. Each experiment included three biological replicates. Statistic comparisons are based on PA at 32 μ g/mL. * $P \le 0.05$; ** $P \le 0.01$; **** $P \le 0.001$; **** $P \le 0.0001$; ns: not significant by one-way ANOVA with Dunnett's multiple comparisons test.

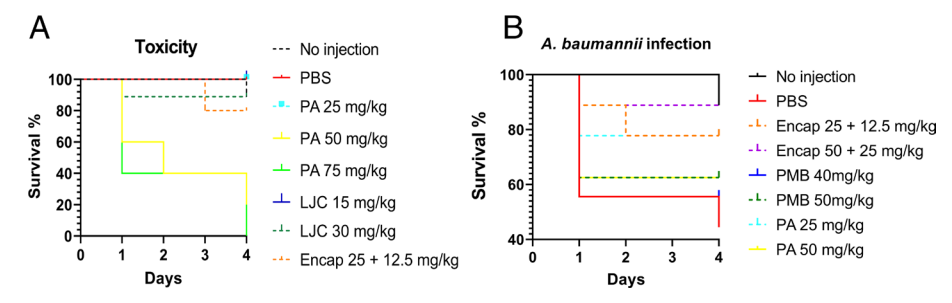


Fig. 7. In vivo study using *G. mellonella*. (*A*) Toxicity of PA and *Encapsulated* approach; (*B*) therapeutic antibacterial effect of PA and *Encapsulation* strategy against *A. baumannii*, respectively. The tests were performed using a bacterial LD₅₀ of 1.5 × 10^6 CFU/mL. PBS: phosphate buffered saline group (untreated control). The mortality was recorded daily over 4 d.

SI Appendix, Figs. S34–S36), LJC at 15 mg/kg or 30 mg/kg (body weight) presented no toxicity (higher concentrations were not tested due to poor aqueous solubility). The PA at 25 mg/kg and *Encapsulation* (25 + 12.5 mg/kg) were also not toxic. As expected, dose escalation of the PA decreased survival. At 50 mg/kg and 75 mg/kg, survival rates at day 4 were 20% and 0%, respectively.

For the infected larvae, 50 mg/kg of PA achieves ~80% survival rate while the Encapsulation (at 50 + 25 mg/kg) increases the survival rate to ~90% (Fig. 7B). Meanwhile, PMB at 50 mg/kg presents a survival rate slightly above 60%. We believe the observed difference may be attributed, at least in part, to variations in pharmacokinetics between PMB and our tested systems. G. mellonella has been shown to provide half-life estimations for antibiotics comparable to those observed in humans (43). PMB is typically cleared from human plasma within 6 h to 24 h based on the administration method (44) and displays a half-life of 9 h to 11.5 h (45), leading to daily administration to patients (46). It is possible a similar effect happens in the worms. Further, our lab has shown that PAs modified with an urea motif are stable in human serum, with over 75% PA remaining after 24 h (47). In our assay, the drugs were administered once at day 0, which might be the reason for the low antimicrobial efficacy of PMB. However, this dose frequency did not influence our Encapsulated samples significantly, which may suggest a better Pharmacokinetic-Pharmacodynamic (PK/PD) profile.

Discussion

Intermolecular cohesion impacts the morphology and physicochemical and biological properties of PA nanostructures. For instance, strong intermolecular cohesion in fibers is associated with improved cell survival (48), whereas weak cohesion in cationic micelles induces cell death (12). Based on these precedents, we designed a urea-modified PA, [C₁₆]uK₂, which may provide the "middle point" for the nanostructure's stability. We hypothesize the interplay between the enhanced molecular cohesion (due to the urea's hydrogen bonding) and the positive surface charge could result in a PA nanostructure that balances antimicrobial activity without affecting human cells. Further, the encapsulation of a hydrophobic molecule may influence the shape of the nanostructures due to changes in the lipid core. The morphology of PA-LJC nanostructures and the location of the encapsulated LJC were assigned using experimental data and MOLT computational modeling. We found that the cargo alters the morphology and stability of the resulting nanostructures. The more cargo that is encapsulated, the more unstable the nanostructure becomes. Our release studies suggested the possibility of controlling the release rate of the encapsulated compound by tuning the nanostructure's stability, which can be beneficial for the optimization of PK/PD properties.

We observed an additive (MRSA JE2) or spectrum broadening (A. baumannii) effect in both dual therapies (Combination and Encapsulation). In addition, relevant changes in the expression of genes related to virulence factors and biofilm formation (particularly the bap gene) were observed with the Combination strategy, consistent with previous reports that dihydrothiazepines affect the expression of virulence factors. These results support our hypothesis that cationic PA nanostructures improve the penetration of LJC. This approach could be applied to the repurposing of antimicrobials that have a narrow therapeutic spectrum due to low intracellular penetration. Moreover, the Encapsulation strategy reduces the MIC value of LJC while achieving a controlled releasing/killing profile.

The availability of LJC and PA molecules is a key difference between the Combination and Encapsulation strategies. This dissimilarity exerts a discernible influence on their respective antimicrobial activities: distinct MICs, diverse killing profiles, and alterations in bacterial membranes, as previously discussed. For the Combination, at µg/mL scale, most of the LJC molecules are readily available in media (as described in *SI Appendix, kinetic morphology study*). Therefore, as the PA induces membrane damage, LJC can be quickly internalized. In the Encapsulation, the nanostructures have an enhanced hydrophobic collapse induced by LJC (this will affect the dynamics of the nanostructures). Consequently, the interactions between PA and bacteria membrane are hindered (the postulated killing-rate determining step), as well as the LJC release from the nanostructure, which slows the antimicrobial effect when compared to the former strategy. This concept was supported by the live/dead assays and membrane microscopy

The TEM micrographs show morphological alterations for the various treatments and incubation times. After 2 h, PA-treated bacteria showed more cytoplasmatic leakage (shrinking and cytoplasmatic low density) than the *Combination* and *Encapsulation* groups (no significant difference between these two). This difference might be a result of the faster killing profile of PAs described above, which is reinforced by the fact that insufficient bacteria pellet was obtained to be imaged after 6 h. After 6 h, the *Combination* shows electron-dense inclusions (not observed in PA 2 h treatment), which might be related to the LJC activity. For the *Encapsulation*, the swollen periplasmatic space is the most notable alteration, which might be resulting from the low amount of PA molecules available to interact with membranes (low MIC dose and slow release).

The ability to display antibacterial activity against high bacterial density is critical to determine the potential of a drug candidate. Based on our results, membrane-acting antimicrobials (PMB, Dapto, and PA) are less affected by the IE when compared to drugs targeting intracellular components (Genta and VCM). Meanwhile, PMB and

PA exhibit better activity than Dapto. We hypothesize that our PA has a similar mechanism of action as PMB (49). Both compounds act on bacterial membranes via electrostatic attractions (charged segment of peptide) and hydrophobic integration (lipid segment of peptide), using single (free) molecules. On the other hand, Dapto mechanism of action requires the formation of Ca²⁺- Dapto aggregates, generating membrane channels that cause the leakage of ions and loss of membrane integrity (50). The morphological alterations observed on the PA-treated samples have also been observed in PMB-treated bacteria (31). A proposed mechanism of PA antimicrobial action is shown in Fig. 8 and compared to PMB and Dapto.

Cell toxicity is a major challenge for antimicrobial PAs (12). Our approach of combining a PA with LJC results in a reduced therapeutic concentration of PA nanostructures in both dual therapies, proving to be beneficial for cell survival, especially for red blood cells. This observation extends to our in vivo experiments. For example, a dose of 50 mg/kg of PA displays high toxicity toward the larvae. However, the *Encapsulation* at 50 + 25 mg (PA:LJC)/kg does not show toxicity and supports ~90% larvae survival after infection. This might be related to the slow disassembly of PA molecules from the nanostructures, influencing their interaction with cell membranes. Therefore, this constant supply of antimicrobials and enhanced stability might explain the wider therapeutic window compared to PMB. This proof of concept may be useful in developing nano systems with PK/PD profile modulation. More in vitro/vivo studies are needed for further optimization of cationic PA nano-formulations.

Both *Combination* and *Encapsulation* provide additive and/or spectrum-broadening effects. The *Combination* strategy has demonstrated to keep the faster killing character of PAs with an improved therapeutic efficacy. Additionally, the *Encapsulation* strategy functions effectively as a delivery vehicle for hydrophobic molecules, addressing water solubility and biodistribution issues, while exhibiting a wide therapeutic window. The killing profile, which is mainly determined by the amount of available PA to interact with the membrane, can

be engineered by optimizing the loading amount of cargo. Further, we have shown how different formulation approaches result in divergent activity and toxicity profiles. In conclusion, a multifunctional platform has been established using a versatile bioactive PA. The presented systems can be combined with narrow-spectrum, mildly toxic, or metabolically unstable antibiotics enhancing their action and/or addressing their current limitations.

Materials and Methods

Synthesis and Purification. PA was synthesized using standard Fmoc solid-phase peptide chemistry, purified by prep-HPLC (0 to 100% gradient acetonitrile/water), and confirmed by MALDI. LJC (synthetic route presented in *SI Appendix*) was purified by flash column chromatography (gradient hexanes/ethyl acetate, 0 to 100%) and confirmed by MALDI and NMR. Detailed design and description are provided in *SI Appendix*.

Preparation of Molecular Assemblies. 1) PA alone: Lyophilized PA powder was dissolved in HPLC grade water to desired concentration, annealed at 80 °C for 2 h, slowly cooled down to room temperature and aged overnight. 2) *Encapsulation* formulation: Freshly prepared PA solution and LJC solution were mixed, annealed, and aged overnight. 3) *Combination* formulation: LJC solution was added to preformed PA nanostructures and the experiment was performed immediately after. Details are given in *SI Appendix*.

Drug Release Studies. 1) Filtration method: An aliquot of sample was taken from the *Encapsulation* solution at different time points and filtered by a 0.45 μ m filter to a preweighted tube. The sample was lyophilized and weighted. The data at time 0 h was considered as 0% release. 2) DCM-aqueous phase method: 1 mL of DCM was added slowly to 1 mL of the *Encapsulation* solution. At different time points, the DCM layer was replaced with fresh DCM. The removed aliquot was injected into the analytical HPLC and analyzed by gradient 0 to 100% methanol/water. The area under the curve was determined and fitted into a standard curve to calculate the concentration of LJC release. More details are provided in *SI Appendix*.

Computational Modeling. Theoretical modeling was performed using a molecular theory (MOLT) for PA self-assembly. MOLT explicitly incorporates the chemical

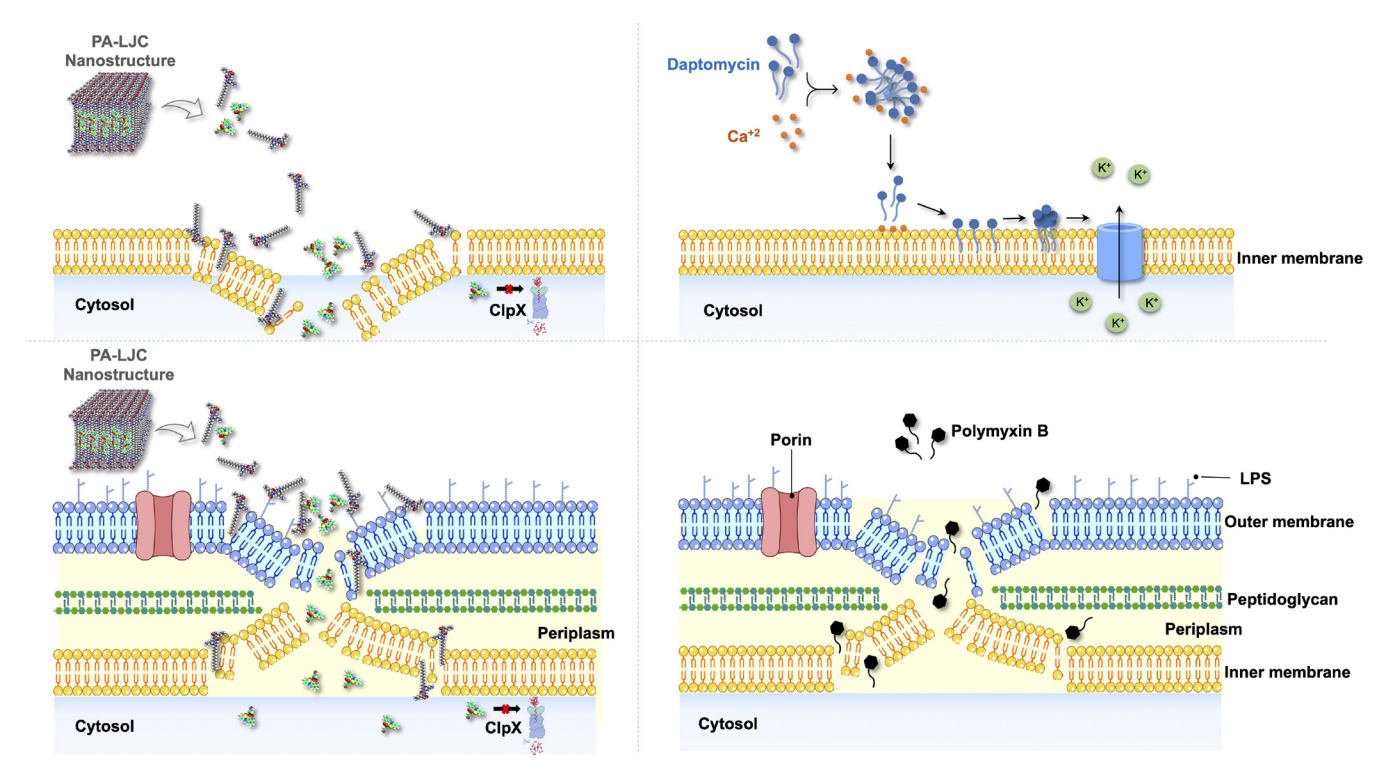


Fig. 8. Proposed mechanism of action for our cationic PA dual therapies on the bacterial surface compared with two membrane-targeting clinically used AMP: daptomycin and PMB.

structure of the different molecules found in the system (at a coarse-grain level), as well as the different interactions and the presence of acid-based chemical equilibrium. As an output, the theory provides structural and thermodynamic information about the system. The references and theoretical approaches are detailed in SI Appendix.

NMR. Samples were prepared in D₂O and maintained at 25 °C during data acquisition. Data were obtained on a Bruker 600 MHz Avance III HD spectrometer equipped with a 5 mm 3-channel (CHN) cryoprobe and Z-gradient pulsing. The solutions were prepared on a mg/mL scale to meet the sensitivity requirements of the NMR instrument. The concentration of PA and LJC (8 + 0.5 mg/mL) is consistent with the ratio of 16:1, as used for the characterization studies. For the Encapsulation samples, a maximum of 1% d₆-DMSO in D₂O was used. For the Combination samples, different ratios of d₆-DMSO in D₂O were tested (as described in SI Appendix).

Microbiological Assays. 1) Antimicrobial activity determination: The minimum inhibitory concentration (MIC) values were determined using the broth microdilution method. The MIC determination assays, and checkerboard assay were determined with a final bacteria density of 1.5×10^5 CFU/mL. A volume of 90 μ L of drug diluted in MHB or cation adjusted MHB (for Daptomycin determinations) and 10 μ L of bacteria suspension in saline (0.85%) were added to a 96-well plate. The plates were incubated for 18 h at 37 °C. Absorbance readings were measured with a 470 nm filter using a multiscan FC microplate photometer. 2) IE: 20 μL of samples were added to 80 µL of bacteria suspension to reach a final density from 10^5 to 10^8 CFU/mL. The plates were incubated at 37 °C and the absorbance was read at 600 nm after 18 to 22 h. The MIC-fold change for the Combination dual therapy strategy was calculated based on the increase fold on the FICi. More details are provided in *SI Appendix*.

Live/Dead Assays. A. baumannii at 10⁶ CFU/mL was treated with [C₁₆]uK₂, LJC, Combination, and Encapsulation strategies for 2 h at 37 °C with shaking (75 rpm). The bacteria suspension was centrifuged at 4,500 rpm for 15 min and stained with DAPI (final concentration 100 μ g/mL) and PI (final concentration 1 μ g/mL) for a final volume of 0.2 mL in PBS. 1) Confocal microscopy: 10 µL stained solution was dropped in the center of a glass slide, covered with coverslips, and then sealed with nail painting. Images were acquired on a Zeiss LSM 800 using a 64× lens objective. 2) A dead bacteria control was used (death induced by heat-shock, 70 °C for 30 min). Samples were analyzed using a LSR II flow cytometer. More details are provided in SI Appendix.

Membrane Studies. A. baumannii cells were washed and resuspended in 5 mM HEPES and 20 mM glucose (pH 7.4). 1) Membrane permeability assay: A final concentration of 7.5 µg/mL propidium iodide (PI) was added to the samples and incubated for 30 min at 37 °C. After the treatment, the fluorescence intensity was monitored for 60 min with 2 min interval at an excitation wavelength of 535 nm and an emission wavelength of 615 nm using a fluorescence plate reader 2) Membrane potential assay: A final concentration of 1 µM of 3,3'-dipropylthiadicarbocyanine iodide ([DiSC3(5)]) was added to the samples and incubated for 30 min at 37 °C. After the treatment, the fluorescence intensity was monitored for 60 min with 2 min interval at an excitation wavelength of 622 nm and an emission wavelength of 670 nm using a fluorescence plate reader. More details are provided in *SI Appendix*.

Membrane Microscopy Studies. A. baumannii at 10⁸ cells/mL were treated with [C₁₆]uK₂, LJC, the Combination or the Encapsulation solutions for 2 h at 37 °C, shaking at 75 rpm. 1) SEM: The suspension was washed with saline and fixed by immersion in a solution of 2% glutaraldehyde, 2% paraformaldehyde in a 0.1 M Sorenson's phosphate buffer (pH 6.2) for a minimum of 24 h at 4 °C. Samples were then washed, postfixed in a 1% agueous solution of osmium tetroxide and dried at critical point. The following day, samples were coated and imaged at 30 kV in a FEI Quanta 200 SEM operating in high vacuum mode. 2) Confocal Microscopy: The bacteria suspension was centrifuged at 4,500 rpm for 15 min and stained with the membrane staining FM4-64 (1.5 µM) and Syto 9 (1.0 µM) for a final volume of 0.2 mL in PBS. Images were acquired on a Zeiss AxioImager.Z2 equipped with an Apotome2 using a 100 × lens objective. 3) AFM: The suspension was washed with saline and fixed with 4% paraformaldehyde at room temperature for 30 min. Mica was treated with 0.5% gelatin and dried for several hours at ambient conditions. A total of $4 \mu L$ of fixed bacteria was deposited and dried out at ambient condition for about 15 min. Scans were collected on MultiMode Nanoscope four in the tapping mode in air. 4) TEM (bacterial membrane analysis): The suspensions were washed with and fixed by immersion in a solution of 2% glutaraldehyde, 2% paraformaldehyde in a 0.1 M Sorenson's phosphate buffer (pH 7.2) for a minimum of 24 h at 4 °C. Samples were then washed, postfixed, and dehydrated. Thin sections (90 nm) made with Leica UC7 Ultracut ultramicrotome were placed on 200 mesh copper grids, poststained with 2% Uranyl Acetate followed by Reynolds Lead Citrate and examined on a Tecnai G² Spirit TWIN (FEI) operating at an accelerating voltage of 80 kV. Images were acquired digitally with an AMT digital imaging system. More details are provided in SI Appendix.

Cell Culture. HEK 293T and Hep-2 were cultured using ATCC protocols and passages 3 to 8 were used for all the experiments. The cytotoxicity was accessed by XTT assays.

Hemolysis Study. 1 mL of freshly extracted mice blood (stored in a heparin tube) was centrifuged at 1,200 rpm for 10 min at 4 °C and washed three times with PBS. The cells were resuspended in 4 mL PBS. Next, 40 µL of samples, 120 µL of PBS, and 40 µL of mice blood were added to each well in a 96-well plate. The plate was incubated for 1 h in the incubator (5% CO2, 37 °C), followed by centrifuging at 2,500 rpm for 10 min. A volume of 70 µL of the suspension was transferred to new wells and read at 540 nm. Cells treated with 1% Triton X-100 were used as the control which presents 100% hemolysis.

In Vivo Antibacterial Studies. Five to nine (depending on the determination) healthy larvae (160 to 260 mg each) were selected for each step in the procedure. The bacteria suspension (A. baumannii) was injected into the last left proleg (Hamilton neurons syringe 25 μL, 33 gauge, point style 4, angle 12°). The larvae were incubated at 37 °C for 2 to 4 d and mortality was recorded daily. More details are provided in SI Appendix.

Data, Materials, and Software Availability. Raw data for SEM, confocal microscopy, flow cytometry experiments and code for the theoretical modeling simulation are available from figshare repository (https://doi.org/10.6084/ m9.figshare.25404133) (51). All other data are included in the manuscript and/ or SI Appendix.

ACKNOWLEDGMENTS. Research reported in this publication was supported by the U.S.-Egypt Science and Technology Joint Fund with funding provided by the United States Agency for International Development through the National Academies of Sciences, Engineering, and Medicine (National Academies) award # 72026321CA00001 and by the NSF CAREER Award # DMR-1941731 (M.C.-S. PI on both). H.X. and L.J.d.C. thank support from the University of Nebraska Medical Center (UNMC) graduate studies fellowship. M.T. acknowledges financial support from ANPCyT PICT 1520-2019. This work used resources from the Holland Computing Center of the University of Nebraska, which receives support from the University of Nebraska-Lincoln (UNL) Office of Research and Economic Development, and the Nebraska Research Initiative. We acknowledge the NMR (E. Ezell) and the TEM (T. Bargar and N. Conoan) Core Facilities. We thank Drs. S. G. Romanova and P. Kakalii Center for Drug Delivery & Nanomedicine (CDDN-UNMC) for assistance. Further, we thank Dr. S. P. Ouellette and Dr. J. Lee from UNMC for their help with confocal microscopy. We thank Dr. D. Ronning for help with the inoculum studies.

Author affiliations: ^aDepartment of Pharmaceutical Sciences, College of Pharmacy, University of Nebraska Medical Center, Omaha, NE 68198; ^bInstituto Nacional de Tecnología Industrial, Micro y Nanotecnologías, San Martín, Buenos Aires B1650WAB, Argentina; ¹Universidad de Buenos Aires, Facultad de Ciencias Exactas y Naturales, Departamento de Química Inorgánica Analítica y Química Física, Pabellón 2, Ciudad Universitaria, Ciudad Autónoma de Buenos Aires C1428, Argentina; ^dUniversidad de Buenos Aires-Consejo Nacional de Investigaciones Cientificas y Tecnicas, Facultad de Ciencias Exactas y Naturales, Instituto de Quimica de los Materiales, Ambiente y Energia, Pabellon 2, Ciudad Universitaria, Ciudad Autonoma de Buenos Aires C1428; and ^eDepartment of Pharmaceutical Sciences, Lloyd L. Gregory School of Pharmacy, Palm Beach Atlantic University, FL 33401

- EClinicalMedicine, Antimicrobial resistance: A top ten global public health threat. EClinicalMedicine 41, 101221 (2021).
- R. E. Baker et al., Infectious disease in an era of global change. Nat. Rev. Microbiol. 20, 193-205
- J. Conly, B. Johnston, Where are all the new antibiotics? The new antibiotic paradox. Can. J. Infect. Dis. Med. Microbiol. 16, 159-160 (2005).
- H. Cui, M. J. Webber, S. I. Stupp, Self-assembly of peptide amphiphiles: From molecules to nanostructures to biomaterials. Biopolymers 94, 1-18 (2010).
- B. Findlay, G. G. Zhanel, F. Schweizer, Cationic amphiphiles, a new generation of antimicrobials inspired by the natural antimicrobial peptide scaffold. Antimicrob. Agents Chemother. 54, 4049-4058 (2010).
- L. Y. Zakharova et al., Cationic surfactants: Self-assembly, structure-activity correlation and their 6. biological applications. Int. J. Mol. Sci. 20, 5534 (2019).
- R. Karstad, G. Isaksen, B. O. Brandsdal, J. S. Svendsen, J. Svenson, Unnatural amino acid side chains as S1, S1', and S2' probes yield cationic antimicrobial peptides with stability toward chymotryptic degradation. J. Med. Chem. 53, 5558-5566 (2010).
- A. Mozhi, I. Ahmad, C. I. Okeke, C. Li, X.-J. Liang, pH-sensitive polymeric micelles for the Codelivery of proapoptotic peptide and anticancer drug for synergistic cancer therapy. RSC Adv. 7, 12886-12896 (2017).
- M. J. Webber et al., Development of bioactive peptide amphiphiles for therapeutic cell delivery. Acta Biomater. 6, 3-11 (2010).
- T. J. Moyer et al., pH and amphiphilic structure direct supramolecular behavior in biofunctional assemblies. J. Am. Chem. Soc. 136, 14746-14752 (2014).
- 11. M. C. Morris, J. Depollier, J. Mery, F. Heitz, G. Divita, A peptide carrier for the delivery of biologically active proteins into mammalian cells. Nat. Biotechnol. 19, 1173-1176 (2001).
- N. Rodrigues de Almeida et al., Design, synthesis, and nanostructure-dependent antibacterial activity of cationic peptide amphiphiles. ACS Appl. Mater. Interfaces 11, 2790-2801 (2019).
- G. Zaldivar et al., Conformal electrodeposition of antimicrobial hydrogels formed by self-assembled peptide amphiphiles. Adv. Mater. Interfaces 10, 2300046 (2023).
- C. Fetzer et al., A chemical disruptor of the ClpX chaperone complex attenuates the virulence of multidrug-resistant Staphylococcus aureus. Angew. Chem. Int. Ed. Engl. 56, 15746-15750 (2017).
- M. Sen et al., The ClpXP protease unfolds substrates using a constant rate of pulling but different gears. Cell 155, 636-646 (2013).
- J. K. Kajfasz, J. Abranches, J. A. Lemos, Transcriptome analysis reveals that ClpXP proteolysis controls 16. key virulence properties of Streptococcus mutans. Microbiology 157, 2880-2890 (2011).
- S. C. Kahne, K. H. Darwin, Structural determinants of regulated proteolysis in pathogenic bacteria by ClpP and the proteasome. Curr. Opin. Struct. Biol. 67, 120-126 (2021).
- 18. H. Brötz-Oesterhelt et al., Dysregulation of bacterial proteolytic machinery by a new class of antibiotics. Nat. Med. 11, 1082-1087 (2005).
- E. Leung et al., Activators of cylindrical proteases as antimicrobials: Identification and development of small molecule activators of ClpP protease. *Biol. Chem.* **18**, 1167–1178 (2011).
- G. Zaldivar et al., Molecular theory: A tool for predicting the outcome of self-assembly of polymers, 20. nanoparticles, amphiphiles, and other soft materials. ACS Omega 7, 38109-38121 (2022).
- 21. G. Zaldivar, S. Vemulapalli, V. Udumula, M. Conda-Sheridan, M. Tagliazucchi, Self-assembled nanostructures of peptide amphiphiles: Charge regulation by size regulation. J. Phys. Chem. C 123, 17606-17615 (2019).
- G. Zaldivar, M. Conda-Sheridan, M. Tagliazucchi, Molecular basis for the morphological transitions of surfactant wormlike micelles triggered by encapsulated nonpolar molecules. Langmuir 37, 3093-3103 (2021).
- G. Zaldivar, M. Conda-Sheridan, M. Tagliazucchi, Scission energies of surfactant wormlike micelles loaded with nonpolar additives. J. Colloid Interface Sci. 604, 757-766 (2021).
- R. Ridolfo et al., Exploring the impact of morphology on the properties of biodegradable nanoparticles and their diffusion in complex biological medium. Biomacromolecules 22, 126-133
- L. Avram, Y. Cohen, Diffusion NMR of molecular cages and capsules. Chem. Soc. Rev. 44, 586-602 (2015).
- N. S. Lee et al., Influence of nanostructure morphology on host capacity and kinetics of guest release. Small 7, 1998-2003 (2011).

- 27. M. J. Hall, R. F. Middleton, D. Westmacott, The fractional inhibitory concentration (FIC) index as a measure of synergy. J. Antimicrob. Chemother. 11, 427-433 (1983).
- C. D. Doern, When does 2 plus 2 equal 5? A review of antimicrobial synergy testing. J. Clin. Microbiol. 52, 4124-4128 (2014).
- L. C. Crowley et al., Measuring cell death by propidium iodide uptake and flow cytometry. Cold Spring Harb. Protoc. 7, (2016).
- 30. A. Sahalan, A. Aziz, H. Hing, M. K. Abd Ghani, Divalent CATIONS (Mg2+, Ca2+) protect bacterial outer membrane damage by polymyxin B. Sains Malays. 42, 301-306 (2013).
- F. Rabanal et al., A bioinspired peptide scaffold with high antibiotic activity and low in vivo toxicity. Sci. Rep. 5, 10558 (2015).
- K. A. Brossard, A. A. Campagnari, The Acinetobacter baumannii biofilm-associated protein plays a role in adherence to human epithelial cells. Infect. Immun. 80, 228-233 (2012).
- K. I. Udekwu, N. Parrish, P. Ankomah, F. Baquero, B. R. Levin, Functional relationship between bacterial cell density and the efficacy of antibiotics. J. Antimicrob. Chemother. 63, 745-757 (2009).
- C. König, H. P. Simmen, J. Blaser, Bacterial concentrations in pus and infected peritoneal fluidimplications for bactericidal activity of antibiotics. J. Antimicrob. Chemother. 42, 227-232 (1998).
- W. R. Miller et al., The cefazolin inoculum effect is associated with increased mortality in methicillinsusceptible Staphylococcus aureus bacteremia. Open Forum Infect. Dis. 5, ofy123 (2018).
- I. Greco et al., Correlation between hemolytic activity, cytotoxicity and systemic in vivo toxicity of synthetic antimicrobial peptides. Sci. Rep. 10, 13206 (2020).
- L. Lin et al., Membrane-disruptive peptides/peptidomimetics-based therapeutics: Promising systems to combat bacteria and cancer in the drug-resistant era. Acta Pharm. Sin. B 11, 2609-2644 (2021).
- 38. A. C. Alves, D. Ribeiro, C. Nunes, S. Reis, Biophysics in cancer: The relevance of drug-membrane interaction studies. Biochim. Biophys. Acta 1858, 2231-2244 (2016).
- O. V. Bondar, D. V. Saifullina, I. I. Shakhmaeva, I. I. Mavlyutova, T. I. Abdullin, Monitoring of the zeta potential of human cells upon reduction in their viability and interaction with polymers. Acta Naturae 4, 78-81 (2012).
- K. Amin, R. M. Dannenfelser, In vitro hemolysis: Guidance for the pharmaceutical scientist. J. Pharm. Sci. 95, 1173-1176 (2006).
- G. Ménard, A. Rouillon, V. Cattoir, P.-Y. Donnio, Galleria mellonella as a suitable model of bacterial infection: Past, present and future. Front. Cell. Infect. Microbiol. 11, 782733 (2021).
- K. Ignasiak, A. Maxwell, Galleria mellonella (greater wax moth) larvae as a model for antibiotic susceptibility testing and acute toxicity trials. BMC Res. Notes 10, 428 (2017).
- 43. L. Hill, N. Veli, P. J. Coote, Evaluation of Galleria mellonella larvae for measuring the efficacy and pharmacokinetics of antibiotic therapies against Pseudomonas aeruginosa infection. Int. J. Antimicrob. Agents 43, 254-261 (2014).
- K. D. Roberts et al., A synthetic lipopeptide targeting top-priority multidrug-resistant Gram-negative pathogens. Nat. Commun. 13, 1625 (2022).
- S. N. Avedissian et al., A review of the clinical pharmacokinetics of polymyxin B. Antibiotics 8, 31 (2019).
- 46. A. A. Pastewski et al., Parenteral polymyxin B use in patients with multidrug-resistant gramnegative bacteremia and urinary tract infections; A retrospective case series, Ann. Pharmacother. 42. 1177-1187 (2008).
- 47. H. Xing et al., Urea-modified self-assembling peptide amphiphiles that form well-defined nanostructures and hydrogels for biomedical applications. ACS Appl. Bio Mater. 5, 4599–4610
- C. J. Newcomb et al., Cell death versus cell survival instructed by supramolecular cohesion of nanostructures. Nat. Commun. 5, 3321 (2014).
- S. S. Mohapatra, S. K. Dwibedy, I. Padhy, Polymyxins, the last-resort antibiotics: Mode of action, resistance emergence, and potential solutions. J. Biosci. 46, 85 (2021).
- A. Baran, A. Kwiatkowska, L. Potocki, Antibiotics and bacterial resistance-A short story of an endless arms race. Int. J. Mol. Sci. 24 (2023).
- 51. L. de Campos et al., Raw data for SEM, confocal microscopy, flow cytometry experiments and code for the theoretical modeling simulation from the article: "Engineering a nano antibiotic system displaying dual mechanism of action", Figshare. https://doi.org/10.6084/m9.figshare.25404133. v1. Accessed 26 March 2024.

12 of 12 https://doi.org/10.1073/pnas.2321498121